Interfacial room temperature magnetism and enhanced magnetocaloric effect in strained $La_{0.66}Ca_{0.34}MnO_3/BaTiO_3$ heterostructures

N. S. Bingham,[1,2,*] A. K. Suszka,[1,2,†] C. A. F. Vaz,[3] H. Kim,[4] and L. J. Heyderman[1,2]
[1]*Laboratory for Mesoscopic Systems, Department of Materials, ETH Zürich, 8093 Zürich, Switzerland*
[2]*Laboratory for Micro and Nano Technology, Paul Scherrer Institut, 5232 Villigen PSI, Switzerland*
[3]*Swiss Light Source, Paul Scherrer Institut, 5232 Villigen PSI, Switzerland*
[4]*Naval Research Laboratory, Washington, DC 20375, USA*
(Received 25 May 2016; revised manuscript received 31 May 2017; published 13 July 2017)

We present a modification of the magnetization and an electronic reconfiguration due to interfacial coupling between strain relaxed $La_{0.66}Ca_{0.34}MnO_3$ and ultrathin $BaTiO_3$ films using the magnetocaloric effect and photoemission electron microscopy at the Mn, Ti $L_{2,3}$ edges. The addition of a top $BaTiO_3$ layer leads to strain-induced enhancement of the magnetocaloric effect in $La_{0.66}Ca_{0.34}MnO_3$, due to the structural transitions in $BaTiO_3$, and to room temperature ferromagnetism due to electronic reconfiguration at the interface.

DOI: 10.1103/PhysRevB.96.024419

I. INTRODUCTION

The venerable perovskite manganites ($R_{1-x}A_xMnO_3$) have generated immense interest since their discovery in the 1950s [1,2] due to the complex interplay between competing magnetic, electronic, and structural degrees of freedom. Such interplay leads to interesting phenomena such as colossal magnetoresistance (CMR) [3], multiferroicity [4], charge ordering [5,6], and a variety of magnetic properties [7]. Zener's double exchange model was initially proposed [8] in order to explain these order parameters, where Mn^{3+} and Mn^{4+} ions exchange charge carriers via the oxygen $2p$ orbitals. However, this theory fails to accurately predict the role of the lattice, as well as CMR behavior [9–12]. In order to obtain a better understanding, the role of strong electron-phonon coupling (such as lattice polarons and Jahn-Teller distortion [13]) must be considered.

Recently [14,15], $La_{0.66}Ca_{0.34}MnO_3$ (LCMO) and $La_{0.66}Sr_{0.34}MnO_3$ thin films grown on $BaTiO_3$ (BTO) substrates have been shown to exhibit large jumps in temperature-dependent magnetization and giant magnetocaloric effect (MCE), due to induced strain from first-order structural phase transitions, where BTO changes from rhombohedral to orthorhombic at 183 K, and from orthorhombic to tetragonal at 278 K [16]. This modification is magnified in the LCMO film due to the similarity between the La and Ca ions, which makes LCMO prone to exhibit mesoscopic phase separation due to MnO_6 tilting when subjected to external perturbations. Generally, many of the studies on manganite interfaces involve substrate-induced strain on the magnetic film [17–21]. This results in changes of the film properties with the film adjusting to the in-plane symmetry of the substrate. However, little work has been dedicated to the role of interfacial effects on the bulk film properties.

Interfaces of thin film manganite heterostructures are well-documented sites for fundamentally altered magnetism [22,23]. Superlattices of ferromagnetic and antiferromagnetic layers can lead to an enhancement of the total magnetization through an induced ferromagnetic ordering extending into the otherwise antiferromagnetic layer via charge carrier transfer [24], while ferromagnetism has also been observed at the interfaces between two nominally insulating antiferromagnets [25]. The control of the physical properties of the manganites through charge modulation at the interface with other materials alters the crystal field at the interface of the manganite, thus creating new interactions via tilting of the Mn-O bond angles or hybridization with a nearest (next-nearest) neighbor and an overall redistribution of localized Mn charge.

In these strongly correlated systems, slight changes in the electronic density can modify the overall balance between competing ground states and, in turn, reveal new states not accessible in the bulk [26]. For example, it is predicted that weakly strained films can form nanoscale magnetically and/or electronically ordered clusters [27], two-dimensional electron gases, and superconductivity [28]. While the consequences of interfacial magnetism on the transport properties have been studied in great detail [22,29,30], a clear microscopic understanding of its impact is still lacking due to challenges inherent to the characterization of interfaces.

We report a combined charge carrier transfer and structurally induced modification of the magnetic and electronic properties of an LCMO film by utilizing the structural transitions of a coupled epitaxial BTO layer. The BTO film thickness (5 nm) is chosen such that the tetragonal to orthorhombic phase transition coincides with the magnetic phase transition of LCMO, at 250 K [16]. We show that in such a system, there is a strong enhancement of the magnetocaloric properties in addition to a persistence of interfacial magnetic order at room temperature, which we relate to charge modification at the BTO-LCMO interface. Additionally, such a thin BTO capping layer provides an excellent sample geometry for x-ray photoemission electron microscopy (XPEEM) studies of the LCMO/BTO interface due to an electron escape depth of 5–7 nm.

II. METHODS

In order to fully characterize the macroscopic physical properties of the film, we employ MCE, which describes the

*binghamn@gmail.com; Currently a National Research Council Research Associate at the U.S. Naval Research Laboratory, Washington, DC 20375, USA.
†anna.suszka@psi.ch

adiabatic temperature (isothermal entropy) change due to magnetizing a magnetic material, an effect that has been explored for magnetic refrigeration applications [31]. MCE has also been proven to be a sensitive probe for complex phase transitions [32–34]. However, the calculated absolute value of the magnetic entropy change (ΔS_M) becomes ambiguous at first-order phase transitions, due to the discontinuity in the order parameter. Also detrimental from an application point of view are heat losses due to thermal and magnetic hysteresis associated with first-order transitions [33]. Nevertheless, much information can be gained about magnetic materials using MCE measurements. Since the isothermal MCE is dependent on the derivative of the magnetization, it is inherently more sensitive to small changes in the magnetic properties than standard magnetometry methods. Additionally, one can use the information produced from MCE measurements to determine the order of a transition [35]. MCE is determined by measuring isothermal magnetization (M) versus applied field (H) curves and integrating between the curves using the thermodynamic Maxwell relation to achieve the overall change in magnetic entropy:

$$\Delta S_M = \mu_0 \int \left(\frac{\partial M}{\partial T}\right)_H dH, \tag{1}$$

where μ_0 is the vacuum permeability.

LCMO and BTO films were deposited on MgO (100) substrates via pulsed-laser deposition (PLD) using a pulsed excimer laser (248 nm, pulse width = 20 ns), with commercially obtained polycrystalline targets, at a fixed target-substrate distance of 6 cm and laser fluence of 2 J/cm^2. The substrate temperature during deposition was 1050 K with an O_2 partial pressure of 400 mTorr during deposition. After deposition, the films were annealed at 1050 K for 2 h in 380 Torr O_2 and cooled to room temperature at 5 K/min. The nominal film thickness of LCMO and BTO films is 50 and 5 nm, respectively, confirmed with atomic force and scanning electron microscopy measurements. The choice of MgO substrates ensures a fully strain-relaxed LCMO film [36,37] such that the external strain is purely due to the addition of the BTO capping layer. Magnetometry and magnetocaloric measurements were performed with a commercial (Quantum Design MPMS 3) superconducting quantum interference device (SQUID) magnetometer.

III. RESULTS AND DISCUSSION

X-ray diffraction (XRD) patterns [Fig. 1(a)] show epitaxial growth of both pseudocubic LCMO and tetragonal BTO with no impurity phases. The lattice constants of both films are within 0.2% of the bulk LCMO and BTO values indicating relaxed-epitaxy growth. This is a consequence of the large lattice misfit between MgO and LCMO (~9%), which leads to an abrupt lattice relaxation through lattice defects [36,37]. The addition of these defects in the film can induce phase separation and broaden the transition, which can lead to the conversion of the first-order para-ferromagnetic transition into a second-order transition. The distribution of defects can be qualitatively described by the temperature spread (Γ) of the derivative of the resistivity [32,38]. We find $\Gamma \sim 15$ K [Fig. 1(b)], which is larger than the previously reported [38] value ($\Gamma \sim 5$ K) for single crystalline LCMO. The extra broadening in the transition temperature agrees with the expected large density of defects in the thin film and reduced transition temperature.

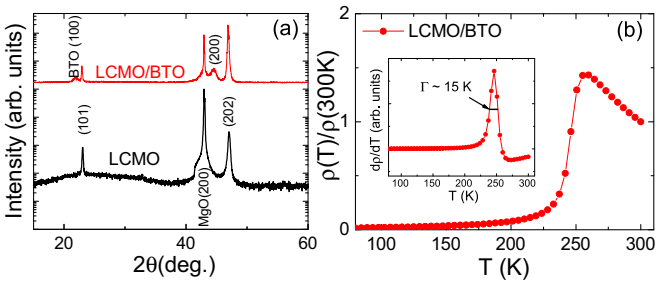

FIG. 1. (a) X-ray diffraction pattern of the LCMO film (bottom curve) and LCMO/BTO heterostructure (top curve). (b) Temperature dependent normalized resistivity measurements for LCMO/BTO bilayer and respective $d\rho/dT$ (inset).

MCE and magnetization measurements [Figs. 2(a) and 2(b)] reveal a ferromagnetic to paramagnetic transition at $T_C \approx$ 250 K both for the plain LCMO film (green circles) as well as for the LCMO capped with BTO (blue triangles), confirming a "bulklike" behavior indicative of strain-relaxed films. The overall magnitude of the change in magnetic entropy (ΔS_M) at T_C is approximately three times larger for the capped film (1.48 J kg^{-1} K^{-1} T^{-1}) than that of the plain LCMO film (0.5 J kg^{-1} K^{-1} T^{-1}) seen in Fig. 2(a) and reported in the literature [14,32,39]. It has been previously shown [32] that the standard first-order magnetic phase transition of LCMO is transformed into a second-order phase transition in the limit of reduced dimensionality. To verify the order of the phase transformation in the LCMO/BTO bilayers, we analyzed the MCE data using two methods. First, we investigated the transition using a purely magnetic measurement approach based on the Banerjee criterion [40]. This criterion states that when a negative slope

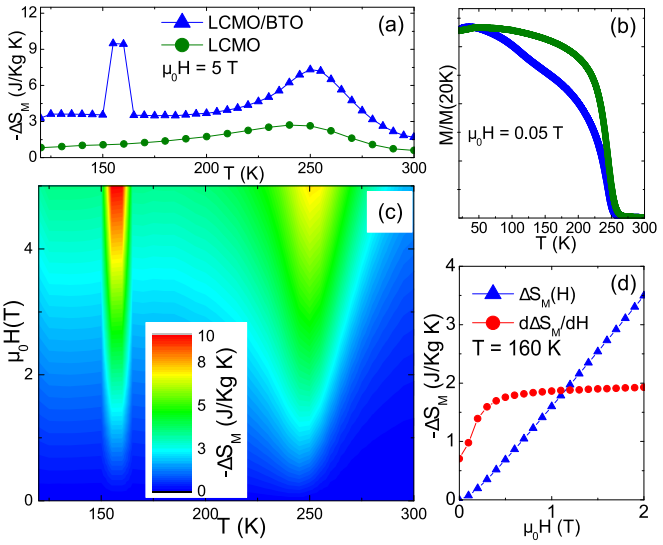

FIG. 2. (a) Magnetocaloric effect and (b) temperature dependent magnetization response of the LCMO/BTO bilayer and plain LCMO samples. (c) Magnetocaloric effect as a function of temperature and magnetic field. (d) Change in magnetic entropy and its derivative as a function of magnetic field.

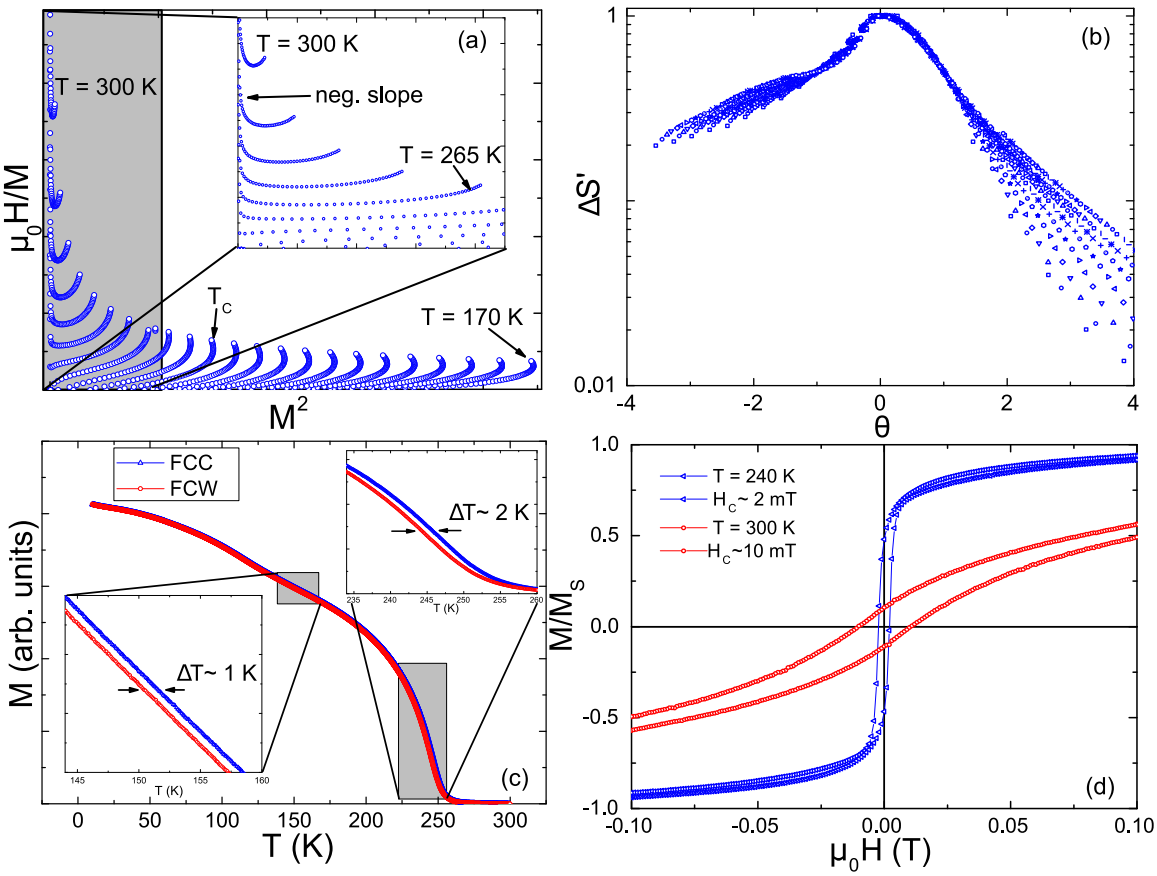

FIG. 3. (a) Isothermal Arrott-Belov curves above and below T_C. (b) Normalized magnetic entropy change near T_C. (c) Field-cooled cooling and field-cooled warming temperature dependent magnetization. (d) Field dependent magnetization at 300 K (red circles) and 240 K (blue triangles).

above T_C occurs in the isothermal Arrott-Belov plots of H/M versus M^2, the transition is of first order. Otherwise it is a second-order transition. From Fig. 3(a) one can see that above T_C there is a negative slope (marked in the inset) indicative of a first-order transition. However, diamagnetic effects due to the substrate can influence this interpretation. Therefore, another test is required. We employed the relatively new method [41,42] based on rescaling ΔS_M curves such that they all collapse onto one single curve for various applied field (H) values at a second-order phase transition. At a first-order phase transition, however, the underlying assumptions break down and there will be a slight spreading of the curves upon renormalization. Therefore, this is an ideal method for checking the order of magnetic transitions. The ΔS_M curves are normalized such that $\Delta S' = \Delta S_M/\Delta S_{\mathrm{Max}}$, where ΔS_{Max} is the peak value for each ΔS_M curve at each H value. Then the temperature is renormalized as

$$\theta = \begin{cases} -(T - T_C)/(T_{r1} - T_C) & \text{if } T \leqslant T_C, \\ (T - T_C)/(T_{r2} - T_C) & \text{if } T \geqslant T_C, \end{cases} \qquad (2)$$

where the reference temperatures (T_{r1}, T_{r2}) are chosen such that $\Delta S_M(T_{r1}) = \Delta S_M(T_{r2}) = \Delta S_{\mathrm{Max}}/2$. Clear separation in the curves, for $|\theta| > 1$ [Fig. 3(b)] and a considerable increase in ΔS_M [Figs. 2(a) and 2(c)] indicate a first-order nature of the phase transition in the BTO capped film.

At ≈150 K, BTO undergoes another structural transition from orthorhombic to rhombohedral, which is found to induce a giant change in both the magnetic entropy as well as the magnetization of the bilayer [Figs. 2(a) and 2(c)]. It is important to note that the magnitude of ΔS_M at 150 K (≈2 J kg^{-1} K^{-1} T^{-1}) is considerably reduced from the values reported for LCMO on BTO substrates (≈9 J kg^{-1} K^{-1} T^{-1}) [14]. This is likely due to enhanced strain coupling between the clamped LCMO film and a single-crystalline BTO substrate. However, by straining LCMO from a cap layer, we provide an easier procedure for fabrication and tuning the magnetocaloric properties. At this transition temperature there is a sudden drop in the lattice parameters of BTO [43] that produces an interfacial change in the LCMO. This is compensated through the rest of the film by a sudden change in the magnetocrystalline anisotropy. The shift of the magnetic anisotropy can be compensated for by the application of a magnetic field of about 1 T, thus leading to a saturation of $\partial \Delta S_M/\partial H$ [Fig. 2(d)]. Interestingly, in spite of the first-order nature of the transitions, there is minimal thermal and magnetic hysteresis [Figs. 3(c) and 3(d)] which is beneficial for magnetic refrigeration applications [33].

While information on the macroscopic magnetization can be gained from MCE measurements, interfacial properties are not easily decoupled from bulk properties, thus requiring a more local probe. It has been shown that colossal effects, such as CMR and colossal MCE, are enhanced when the

material is in a phase-separated state, due to the rapid expansion of one phase that dominates over the other on application of a magnetic field [44–46]. Therefore, in order to fully understand phenomena induced at the interface, we employed x-ray absorption spectroscopy (XAS) combined with x-ray magnetic circular dichroism (XMCD), and x-ray linear dichroism (XLD). In particular XPEEM, based on the photoemission of electrons due to the absorption of x rays, offers spatially resolved element-specific XAS, XMCD, and XLD measurements. The small escape depth of the photoemitted electrons (5–7 nm) provides a means to investigate magnetic, structural, and electronic states at the interface between the two films.

The XAS images were normalized pixelwise to a pre-edge off-resonance image. XMCD and XLD images were calculated using the normalized XAS for circular right (I_R), circular left (I_L), linear horizontal (I_H), and linear vertical (I_V) polarized light and taking their difference over their sum $(I_R - I_L)/(I_R + I_L)$ and $(I_H - I_V)/(I_H + I_V)$, respectively. The data were obtained at the Ti $L_{2,3}$ edges and Mn $L_{2,3}$ edges. XAS and XLD measurements were performed in the magnetically virgin state, while XMCD was measured at remanence after saturating the samples with a magnetic field.

There is a noticeable difference in the XAS between the plain LCMO (without the BTO cap) and the BTO capped films [Fig. 4(a)]. The XAS of the plain LCMO film (black circles) looks similar to that reported in the literature, where the peak at the L_3 edge (642 eV) is associated with the Mn being in a mixture of Mn^{3+} and Mn^{4+} electronic states. The capped film, however, looks drastically different, with primary electronic contributions associated with Mn^{2+}. It is well known that there is a tendency for formation of Mn^{2+} at a manganite interface [47]. In order ensure the Mn^{2+} valence state was not caused by prolonged exposure to air, the films were placed under vacuum after growth until the measurements were performed. As a

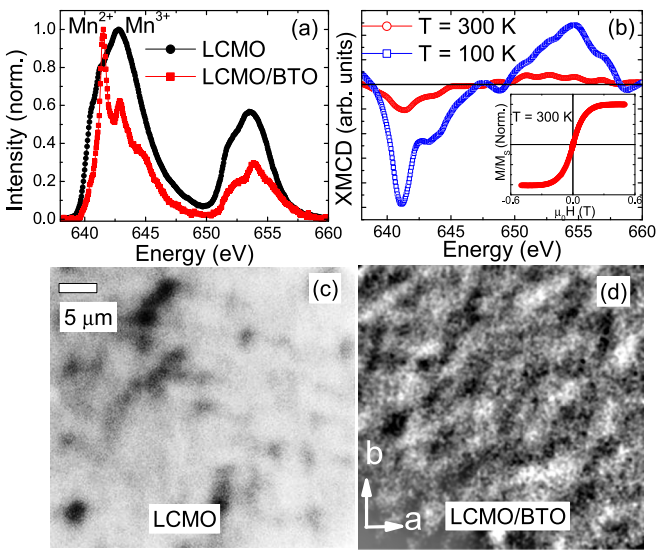

FIG. 4. (a) XAS of LCMO and LCMO with BTO cap at the Mn $L_{2,3}$ edge. (b) XMCD at both low temperature and room temperature for BTO capped LCMO and M vs H at 300 K for the capped film (inset). (c) and (d) XMCD images at $T = 100$ K and $E = 642.5$ eV of LCMO and LCMO/BTO, respectively.

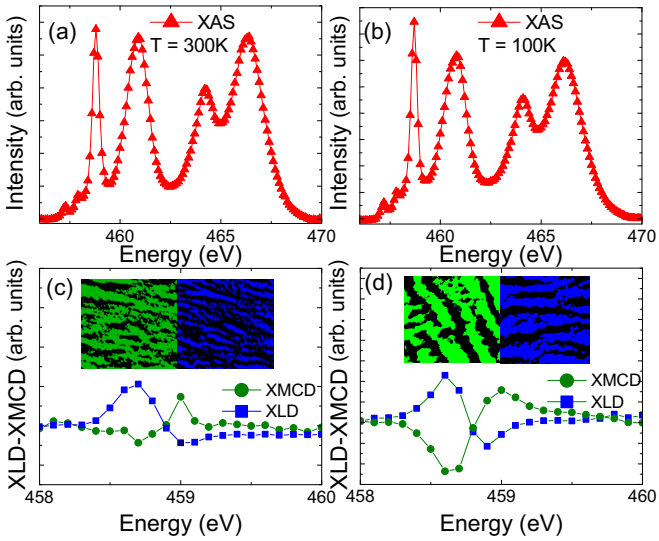

FIG. 5. (a) XAS for BTO/LCMO at (a) 300 K and (b) 100 K. Linear and circular dichroism at the Ti $L_{2,3}$ edge for BTO/LCMO sample at (c) 300 K and (d) 100 K. Insets are the autocorrelation of the XMCD (left panel) and XLD (right panel) partial maps at 300 and 100 K, respectively.

further check, the films were also left in air for two months and, on second measurement, the results were identical, indicating that the altered electronic state is a result of electron doping at the interface. XMCD measurements were performed at 300 and 100 K [Fig. 4(b)], demonstrating that the bilayer sample is clearly ferromagnetic at room temperature, in agreement with the SQUID data [Fig. 4(b) inset]. XPEEM images taken at ≈100 K [Figs. 4(c) and 4(d)] reveal that LCMO exhibits a randomly oriented magnetic domain pattern, while the capped film appears to exhibit domains with preferential orientation along the BTO [110] crystal direction as predicted [16].

To investigate the electronic modifications further, XAS, XMCD, and XLD were also measured at the Ti $L_{2,3}$ edges [Figs. 5(a)–5(d)] both at room temperature and low temperature. The change in the relative intensities between the room temperature [Fig. 5(a)] and low temperature [Fig. 5(b)] measurements is indicative of the BTO structure transition [48]. At room temperature, we see a clear XMCD signal [Fig. 5(c)]. BTO typically exhibits the fundamentally *nonmagnetic* Ti^{4+} electronic configuration. However, since we observe a clear XMCD signal at both low and room temperatures, it follows that the interfacial Ti atoms are in a modified electronic state, leading to the formation of magnetic Ti^{3+}. We note that the observation of magnetically polarized BTO in contact with a ferromagnetic system is now well documented in the literature [15,49,50]. However, since our films are not clamped to the substrate, we are able to investigate the physical properties on a more fundamental level. For this we performed XLD measurements [Figs. 5(c) and 5(d), blue squares], which is a crucial tool for the investigation of effects related to structural changes, e.g., orbit formation and ferroelectricity [51] by probing the distribution of empty Ti-3d states.

In order to quantify the orbital contribution to the x-ray signal we followed the procedure described in [52,53], and calculated the ratio of holes to electrons (X) at the interface

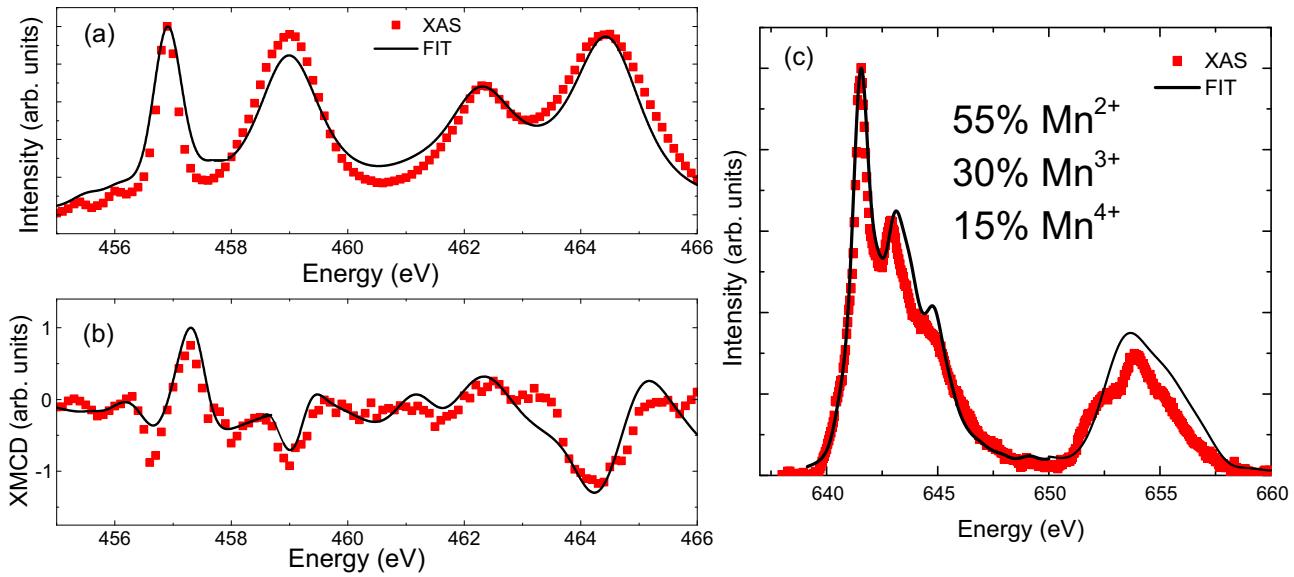

FIG. 6. (a) XAS and (b) XMCD experimental data (red squares) and fit calculated with CTM4XAS for LCMO with BTO cap at the Ti $L_{2,3}$ edge with 11% Ti^{3+}. (c) XAS experimental data and CTM4XAS calculated fit recorded at Mn $L_{2,3}$ edge with 55% Mn^{2+}.

using

$$X = \frac{3\int_{L_{3,2}} I_V(E)dE}{4\int_{L_{3,2}} I_H(E)dE - \int_{L_{2,3}} I_V(E)dE}, \tag{3}$$

where I_V and I_H are the geometrically corrected XAS intensity for the x-ray polarization parallel and perpendicular to the [001] axis of the film, respectively. For a material with predominantly hole doping, $X > 1$, and for electron doping, $X < 1$. For the capped films, we find that the ratio is $X = 0.8$ corresponding to a surplus of electrons at the interface. The electron doping could be due to oxygen vacancies in the LCMO; however, this would result in a larger unit cell which is not evident in the XRD patterns [Fig. 1(a)]. Therefore, the electron doping at the interface is likely due to hybridization between $Mn^{3+/4+}$ and Ti^{4+} electronic states. This results in an enhancement of the $Mn^{2+/3+}$ and Ti^{3+} electronic structure ratio at the interface.

We used the CTM4XAS program [54] to further analyze the Mn and Ti electron valency deduced from XAS/XMCD data in Figs. 4(a), 5(a) and 5(c), respectively. Starting with the Ti $L_{2,3}$ edges, we first simulated the XAS with Ti^{4+} tetragonal symmetry using values from previous studies [55] [Fig. 6(a)]. The experimental peaks are broader than the simulated peaks due to hybridization effects and are dealt with by Lorentz broadening each peak individually. The simulated results for the pure Ti^{4+} exhibits no XMCD signal, as expected. However, with the addition of 11% Ti^{3+} contribution in the simulations we were able to reproduce the XMCD signal [Fig. 6(b)]. Differentiating between Ti^{3+} and Ti^{4+} is not trivial, since the interfacial electronic states exhibit mixed Ti and Mn valency [56] and hybridization between Mn-O-Ti. Nevertheless, we have shown strong evidence for a surplus of electrons at the interface between the two materials likely leading to the formation of nanoscale ferromagnetic and ferroelectric clusters giving rise to the enhancement of the magnetic and electronic properties at the interface. We have also simulated the Mn L edge [Fig. 6(c)] and found that the dominant contribution (55%) is due to Mn^{2+}, whereas the remaining 45% belongs to a nominal mixture of $Mn^{3+/4+}$ at 30% and 15%, respectively. It is important to note that the ratio of Mn^{3+} to Mn^{4+} remains consistent with the expected value for this LCMO stoichiometry.

IV. CONCLUSIONS

In summary, using PEEM, MCE, and magnetometry measurements, we have shown that at epitaxial interfaces between BTO and LCMO there are modifications to the electronic configurations of both the LCMO and BTO. As a result of the interfacial coupling between the two materials there are small scale ferromagnetic correlations above T_C leading to room temperature magnetic ordering. The addition of the BTO capping layer also leads to large MCE at 150 K and an enhancement of the MCE at 250 K due to the orthorhombic-rhombohedral and orthorhombic-tetragonal structural phase transitions in BTO, respectively. By enhancing the MCE via thin-film heterostructures rather than substrate induced effects, we obtained a considerable decrease in magnetic and thermal hysteresis. We have therefore demonstrated a method of strain engineering that enhances the MCE properties. This is a flexible approach that may be applied to enhance and control further phenomena in complex oxide heterostructures such as superconductivity and multiferroicity.

ACKNOWLEDGMENTS

The authors thank Michele Buzzi and Victorino Franco for assistance with measurements and fruitful discussions. Part of this work was performed at the SIM beamline of the Swiss Light Source, Paul Scherrer Institut, Switzerland. A.K.S. acknowledges funding from the European Community's Seventh Framework Program (FP7/2007-2013) under Grant Agreement No. 290605 (COFUND: PSIFELLOW).

[1] G. H. Jonker and J. H. V. Stanten, Physica **16**, 337 (1950).
[2] Y. Tokura and Y. Tomioka, J. Magn. Magn. Mater. **200**, 1 (1999).
[3] S. Jin *et al.*, Science **264**, 413 (1994).
[4] T. Kimura *et al.*, Nature (London) **426**, 55 (2003).
[5] H. Kuwahara *et al.*, Science **270**, 961 (1995).
[6] J. M. D. Coey, M. Viret, L. Ranno, and K. Ounadjela, Phys. Rev. Lett. **75**, 3910 (1995).
[7] M. B. Salamon and M. Jaime, Rev. Mod. Phys. **73**, 583 (2001).
[8] C. Zener, Phys. Rev. **82**, 403 (1951).
[9] A. J. Millis, R. Mueller, and B. I. Shraiman, Phys. Rev. B **54**, 5389 (1996).
[10] A. J. Millis, R. Mueller, and B. I. Shraiman, Phys. Rev. B **54**, 5405 (1996).
[11] A. Moreo *et al.*, Science **283**, 2034 (1999).
[12] A. J. Millis, P. B. Littlewood, and B. I. Shraiman, Phys. Rev. Lett. **74**, 5144 (1995).
[13] H. Röder, J. Zang, and A. R. Bishop, Phys. Rev. Lett. **76**, 1356 (1996).
[14] X. Moya *et al.*, Nat. Mater. **12**, 52 (2013).
[15] W. Eerenstein *et al.*, Nat. Mater. **6**, 348 (2007).
[16] J. Paul, T. Nishimatsu, Y. Kawazoe, and U. V. Waghmare, Phys. Rev. Lett. **99**, 077601 (2007).
[17] Y. K. Yoo *et al.*, Nature (London) **406**, 704 (2000).
[18] K. H. Ahn, T. Lookman, and A. R. Bishop, Nature (London) **428**, 401 (2004).
[19] K. Lai *et al.*, Science **329**, 190 (2010).
[20] P. Orgiani *et al.*, Phys. Rev. B **82**, 205122 (2010).
[21] C. A. F. Vaz, J. A. Moyer, D. A. Arena, C. H. Ahn, and V. E. Henrich, Phys. Rev. B **90**, 024414 (2014).
[22] C. A. F. Vaz *et al.*, J. Phys.: Condens. Matter **24**, 333201 (2012).
[23] P. Zubko *et al.*, Annu. Rev. Condens. Matter Phys. **2**, 141 (2011).
[24] E. Jiménez, J. Camarero, J. Sort, J. Nogués, N. Mikuszeit, J. M. García-Martín, A. Hoffmann, B. Dieny, and R. Miranda, Phys. Rev. B **80**, 014415 (2009).
[25] T. S. Santos, B. J. Kirby, S. Kumar, S. J. May, J. A. Borchers, B. B. Maranville, J. Zarestky, S. G. E. te Velthuis, J. van den Brink, and A. Bhattacharya, Phys. Rev. Lett. **107**, 167202 (2011).
[26] C. A. F. Vaz *et al.*, Adv. Mater. **22**, 2900 (2010).
[27] M. Nagao *et al.*, Nat. Nanotechnol. **8**, 325 (2013)
[28] L. Li *et al.*, Nat. Phys. **7**, 762 (2011).
[29] M. Bibes *et al.*, Adv. Phys. **60**, 5 (2011).
[30] S. Fusil *et al.*, Annu. Rev. Mater. Res. **44**, 91 (2014).
[31] M.-H. Phan and S.-C. Yu, J. Magn. Magn. Mater. **308**, 325 (2007).
[32] P. Lampen *et al.*, Appl. Phys. Lett. **102**, 062414 (2013).
[33] N. S. Bingham *et al.*, J. Appl. Phys. **106**, 023909 (2009).
[34] P. Lampen, N. S. Bingham, M. H. Phan, H. Srikanth, H. T. Yi, and S. W. Cheong, Phys. Rev. B **89**, 144414 (2013).
[35] V. Franco, A. Conde, J. M. Romero-Enrique, and J. S. Blázquez, J. Phys.: Condens. Matter **20**, 285207 (2008).
[36] E. Gommert *et al.*, J. Appl. Phys. **85**, 5417 (1999).
[37] S. R. Singamaneni *et al.*, Appl. Phys. Rev. **3**, 031301 (2016).
[38] M. Egilmez, K. H. Chow, and J. Jung, Appl. Phys. Lett. **92**, 162515 (2008).
[39] X. Zhang *et al.*, Appl. Phys. Lett. **69**, 3596 (1996).
[40] B. K. Banerjee, Phys. Lett. **12**, 16 (1964).
[41] C. M. Bonilla *et al.*, J. Appl. Phys. **107**, 09E131 (2010).
[42] V. Franco, J. S. Blázquez, and A. Conde, Appl. Phys. Lett. **89**, 222512 (2006).
[43] H. Terashita, B. Myer, and J. J. Neumeier, Phys. Rev. B **72**, 132415 (2005)
[44] M. H. Phan, M. B. Morales, N. S. Bingham, H. Srikanth, C. L. Zhang, and S. W. Cheong, Phys. Rev. B **81**, 094413 (2010).
[45] N. S. Bingham, P. Lampen, M. H. Phan, T. D. Hoang, H. D. Chinh, C. L. Zhang, S. W. Cheong, and H. Srikanth, Phys. Rev. B **86**, 064420 (2012).
[46] A. Alberca *et al.*, Sci. Rep. **5**, 17926 (2015).
[47] S. Valencia, A. Gaupp, W. Gudat, Ll. Abad, Ll. Balcells, A. Cavallaro, B. Martinez, and F. J. Palomares, Phys. Rev. B **73**, 104402 (2006).
[48] M. Bugnet, G. Radtke, S. Y. Woo, G.-Z. Zhu, and G. A. Botton, Phys. Rev. B **93**, 020102(R) (2016).
[49] S. M. Wu *et al.*, Nat. Mater. **9**, 756 (2010).
[50] C.-G. Duan, S. S. Jaswal, and E. Y. Tsymbal, Phys. Rev. Lett. **97**, 047201 (2006).
[51] R. V. Chopdekar *et al.*, Phys. Rev. B **86**, 014408 (2012).
[52] C. Schmitz-Antoniak *et al.*, Nat. Commun. **4**, 2051 (2013).
[53] M. Wu *et al.*, Phys. Rev. B **88**, 125124 (2013).
[54] E. Stavitski and F. M. F. de Groot, Micron **41**, 687 (2010).
[55] A. Chassé, S. Borek, K.-M. Schindler, M. Trautmann, M. Huth, F. Steudel, L. Makhova, J. Gräfe, and R. Denecke, Phys. Rev. B **84**, 195135 (2011).
[56] M. Salluzzo *et al.*, Phys. Rev. Lett. **102**, 166804 (2009).